



ELSEVIER

Contents lists available at SciVerse ScienceDirect

Journal of Fluids and Structures

journal homepage: www.elsevier.com/locate/jfs

Shape optimization of a blunt body Vibro-wind galloping oscillator

J.M. Kluger^{a,1}, F.C. Moon^{a,*}, R.H. Rand^{a,b}^a Sibley School of Mechanical and Aerospace Engineering, Cornell University, Ithaca, NY 14850, USA^b Department of Mathematics, Cornell University, Ithaca, NY 14850, USA

ARTICLE INFO

Article history:

Received 7 September 2012

Accepted 25 March 2013

Available online 28 May 2013

Keywords:

Vibro-wind

Galloping instability

Energy harvesting

ABSTRACT

The nonlinear dynamics of a transverse galloping blunt body oscillator is analyzed with respect to its geometric shape and size. The oscillator's equation of motion is studied using an approximation for the lateral aerodynamic force that is a polynomial function of the angle of attack. The harmonic balance method is used to solve the nonlinear differential equation of motion. This solution is used to determine the geometric parameters that minimize its critical wind speed for instability, increase its amplitude sensitivity to wind velocities beyond the critical speed, and minimize or eliminate amplitude hysteresis for increasing and decreasing wind speed. Optimum combinations of blunt body size and shape can be found that best satisfy these desired behaviors. These findings may be useful for creating a reliable, efficient wind energy harvesting system.

© 2013 Published by Elsevier Ltd.

1. Introduction

Several systems of fluid–structure dynamics have been proposed to extract energy from the wind (Bryant and Garcia, 2011; Frayne, 2008; Li and Lipson, 2009; McKinney and DeLaurier, 1981; Moon, 2010a, 2010b; Tang et al., 2008). These systems exploit the unsteady, nonlinear dynamics of blunt body aerodynamics (Moon, 1992; Rand, 2012). As an energy harvester design goal, one desires a geometric shape and size that minimizes the critical wind speed for instability, increases the sensitivity of amplitude to wind velocities beyond the critical speed, and minimizes or eliminates hysteresis with respect to increasing and decreasing wind speeds.

In the Cornell fluid–structure harvester, arrays of cantilevered blunt bodies are assembled in a panel (Moon, 2010b). This system has been called a Vibro-wind energy harvester or Vibro-wind for short. This type of energy harvester lends itself to clean power generation in urban areas, at night, or in wind speeds as low as 2–3 m/s, which are significantly below the 9 m/s start-up velocity of a typical large-scale wind turbine. A Vibro-wind panel occupying one square meter and operating at 10% efficiency in 10 m/s wind might be able to generate 54 W of electricity, a figure on par with solar panels (Moon, 2010a, 2010b). Vibro-wind panels consist of hundreds of centimeter sized bodies (Kuroda and Moon, 2007). In this paper, however, we only examine a single oscillator.

Vibro-wind motion is an example of transverse aerodynamic galloping, the phenomenon of structures with low aspect ratio cross sections developing self-excited oscillations when placed in a fluid flow (Blevins, 1990). These oscillations occur at approximately the natural frequency of the structure. In 1956, Den Hartog used the quasi-steady hypothesis to linearize aerodynamic forces and describe the onset of transverse galloping.

* Correspondence to: Department of Mechanical Engineering, Room 204 Upson Hall, Ithaca, NY 14853, USA. Tel.: +1 607 280 8284; fax: +1 607 255 1222.
E-mail addresses: jociiek@mit.edu (J.M. Kluger), fcm3@cornell.edu (F.C. Moon), rhr2@cornell.edu (R.H. Rand).

¹ Present address: Department of Mechanical Engineering, Massachusetts Institute of Technology, Cambridge, MA 02139, USA.

Nomenclature	
A, B, C, D	coefficients of polynomial approximation to C_{FY}
$\hat{B}=B/A, \hat{C}=C/A, \hat{D}=D/A$	coefficients of polynomial approximation to C_{FY} normalized for A
C_{FY}	lateral aerodynamic force coefficient
depth	blunt body streamwise dimension
f_s	formation frequency of vortices in wake shear layer
h	blunt body characteristic diameter
L	cantilever length
l	blunt body axial length normal to the flow
k	cantilever stiffness
m	effective vibrating mass
m_{BB}	blunt body mass
m_{cant}	cantilever mass
$n=\rho h^2 l/2m$	nondimensionalized mass
r	coefficient of viscous system damping
$St=f_s h/V$	Strouhal number
t	time
$U=V/\omega h$	nondimensionalized air velocity
V	air velocity
$Y=y/h$	nondimensionalized oscillator displacement
$Y'=dY/d\tau$	nondimensionalized oscillator velocity
$\bar{y}=y/h$	nondimensionalized oscillator amplitude
y	blunt body displacement
\bar{y}	blunt body amplitude
$\dot{Y}=dy/dt$	blunt body velocity
α	angle of attack of blunt body relative to wind
$\beta=\theta/(y/L)$	coefficient relating beam tip angle and deflection
δ	isosceles triangle main vertex angle
$\zeta=r/2m\omega$	nondimensionalized damping coefficient
η	ratio of blunt body's rear diameter to front diameter
θ	structural angle
ρ	air density
$\tau=\omega t$	nondimensionalized time
$\omega=\sqrt{k/m}$	natural angular frequency

The quasi-steady hypothesis assumes that the vortex shedding frequency is not in resonance with the natural structural frequency. In the vortex shedding model, there are two nondimensional parameters that characterize the vortex frequency: the Reynolds number, proportional to the velocity; and the Strouhal number, $St=f_s h/V$, where f_s is the frequency of vortex shedding in units of hertz, V is the free stream flow velocity, and h is the cylinder diameter. Characteristics of fluid–structure dynamics have been summarized by [Blevins \(1990\)](#). For obstacles on the order of 20 mm and velocities on the order of 5 m/s, the Reynolds number is around 7000. In this regime, the alternating vortex flow behind a cylinder-type obstacle is well established for a given frequency. One can show that for $10^3 < Re < 10^4$, the range of Reynolds numbers for Vibro-wind systems, $St=0.13$, where $St=f_s h/V$. For an obstacle of width $h=20$ mm and $V=1–5$ m/s, the shedding frequency, f_s , is 7–32 Hz. This paper assumes that f_s does not equal the structural natural frequency of Vibro-wind systems. For the oscillators described in the experimental section of this paper, f_s does not equal the structural natural frequency for the important wind speeds (the critical wind speeds for oscillation and the wind speeds with hysteresis). For structural natural frequencies that do not resonate with the vortex shedding frequency, the aerodynamic forces acting on the oscillating body at any instant are considered equivalent to those acting on a static body with the same angle of attack with respect to the fluid flow ([Blevins, 1990](#); [Den Hartog, 1956](#)). The studies described in this paper use the quasi-steady hypothesis to analyze the dynamics of the body without reference to the details of the aerodynamic flow itself. For information on the fluid flow behind oscillator cylinders, refer to [Luo et al. \(1993\)](#).

Parkinson used the quasi-steady hypothesis to solve the equation of motion for the transverse galloping of a square cylinder. This equation of motion approximated C_{FY} , the nondimensionalized lateral aerodynamic force coefficient, as a seventh-order polynomial of α , the cylinder's angle of attack. Parkinson noted the occurrence of oscillation hysteresis for particular wind speeds ([Parkinson and Smith, 1964](#)). [Van Oudheusden \(1995\)](#) extended Parkinson's analysis to a cylinder undergoing translation coupled with rotation.

Further work has been done to investigate the relationship between oscillator performance and geometry. In 2009, [Barrero-Gil \(2010, Energy Harvesting from Transverse Galloping\)](#) explored the influence of cross section geometry and mechanical properties on the mechanical power of an oscillator. Other studies have related the shape of the lateral aerodynamic force coefficient versus angle of attack curve to system performance. [Barrero-Gil](#) showed that the location and number of inflection points in the $C_{FY}(\alpha)$ curve influence the wind speeds during which the oscillator exhibits hysteresis ([Barrero-Gil et al., 2009](#)). Researchers such as Parkinson, [Barrero-Gil](#), and [Novak](#) have experimentally determined the coefficients in the $C_{FY}(\alpha)$ polynomial approximation for cylinders of various cross sections ([Barrero-Gil, 2010](#); [Novak et al., 1974](#); [Parkinson and Smith, 1964](#)).

The aforementioned studies as well as this paper's analysis are for steady oscillations even though in wind harvesting systems, the wind may be transient or unsteady. Earlier Cornell studies have shown that energy can be harvested from a Vibro-wind array panel in unsteady wind conditions ([Moon, 2010a, 2010b](#)).

This paper discusses the dynamics of an oscillator that is not coupled to an electrical system: the piezoceramic's leads are configured in an open-circuit. The oscillator motion may vary with the inclusion of an energy harvesting device such as a resistor, capacitor, or battery. For example, [Erturk et al. \(2010\)](#) show that coupling a piezoaeroelastic oscillator with a resistor decreases the critical wind speed. Thus, this paper serves as a starting point for understanding the role of oscillator geometry on a piezoaeroelastic energy harvester's performance.

The purpose of this paper is to analytically determine a blunt body cross section with a low critical wind speed, high amplitude sensitivity to wind speed, and minimal hysteresis during galloping that can be used to scavenge energy from the wind.

This paper is organized as follows: The mathematical model governing the oscillator's motion is presented in Section 2. Section 3 describes the results of this model, and Section 4 describes experiments. Then, Section 5 shows the theoretical optimization of critical wind speed, amplitude, and hysteresis as a function of geometry. Finally, this paper's findings are discussed and summarized in Section 6.

2. Model

The Vibro-wind oscillator is a composite structure consisting of a piezoelectric beam cantilevered to a frame at one end and adhered to a steel beam of 0.006-inch thickness at the other end. The free end of the steel beam is inserted into a foam blunt body whose shape is a cylinder of noncircular cross section. The model of this cantilevered oscillator is an extension of the Parkinson and Smith (1964) purely translational oscillator. Both models obey the equation:

$$m\ddot{y} + r\dot{y} + ky = \frac{1}{2}C_{FY}\rho V^2hl, \tag{1}$$

where m is the effective mass of the oscillator, r is the viscous damping, k is the cantilever stiffness, C_{FY} is the lateral aerodynamic force coefficient, ρ is the density of air, V is the wind speed, h is the characteristic dimension of the blunt body normal to the flow, and l is the blunt body axial length normal to the flow (Fig. 1) (Parkinson and Smith, 1964).

Since an appropriate aerodynamic theory defining C_{FY} is unknown, this model uses measured aerodynamic forces from the quasi-steady model. That is, the aerodynamic force acting on a dynamic cylinder in wind speed V , is considered equivalent to the force acting on a static cylinder with the corresponding angle of attack in wind speed V_{rel} . The validity of quasi-steady assumptions for a similar system is described in Van Oudheusden (1995).

Using the quasi-steady theory, the lateral aerodynamic force coefficient, C_{FY} can be approximated as a polynomial on α , the angle of attack:

$$C_{FY} = A\alpha - B\alpha^3 + C\alpha^5 - D\alpha^7. \tag{2}$$

This approximation requires at least a seventh degree polynomial to capture hysteresis behavior (Barrero-Gil et al., 2009; Parkinson and Smith, 1964).

The kinematic relationship between angle of attack, oscillator displacement, and oscillator velocity differs between this model and the Parkinson and Smith model. Fig. 1 depicts the relationship between wind velocity, V , oscillator displacement, y , oscillator velocity, \dot{y} , and structural angle, θ , for a uniform cantilever.

For a uniform cantilevered beam of length L , the relationship between structural angle, θ , and displacement, y , is

$$\theta = \frac{3y}{2L}. \tag{3}$$

Thus, the angle of attack for small \dot{y}/V , such that α can be approximated by $\tan(\alpha)$, is defined as

$$\alpha = \frac{\dot{y}}{V} - \theta = \frac{\dot{y}}{V} - \frac{3y}{2L} = \frac{\dot{y}}{V} - \beta\frac{y}{L}, \tag{4}$$

where the coefficient β can be used for structural designs other than the uniform cantilever. The value of β for the composite cantilevers used in the Cornell Vibro-wind system is described in Section 4.2.4. The angle of attack, α , for a purely translating

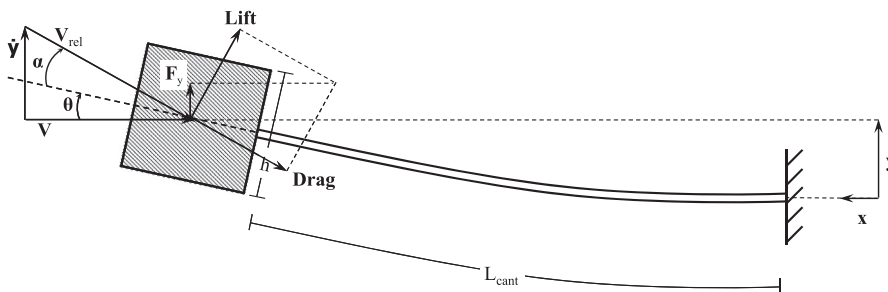


Fig. 1. Model of one-degree-of-freedom galloping for coupled translation and rotation of a uniform cantilevered blunt body oscillator. F_y is the lateral aerodynamic force, *Lift* is aerodynamic lift, *Drag* is aerodynamic drag, y is oscillator displacement, \dot{y} is oscillator velocity, V is wind velocity, V_{rel} is the summation of wind velocity and oscillator velocity, θ is the angle between the blunt body and the wind velocity, α is the angle of attack: the angle between the blunt body and the wind velocity, h is the blunt body diameter, and L_{cant} is the cantilever length.

cylinder is equivalent to Eq. (4) when $\beta=0$:

$$\alpha = \frac{\dot{y}}{V}. \quad (5)$$

It is interesting to note that the expression for angle of attack for an oscillator with one torsional degree of freedom is equivalent to Eq. (4) when $\theta=y/R$, defining R as the radial distance between the rotation axis and the blunt body. In such a system, as described in Van Oudheusden (1995), R remains constant; whereas in our system, radial distance R decreases as the cantilever bends.

3. Analysis and simulation

To analyze the steady-state amplitude of our system in different wind speeds, we nondimensionalize the differential equation of motion, solve it using the method of harmonic balance in *WxMaxima*, a computer algebra program, and plot the resulting expression using the *ezplot* command in *MATLAB* (Rand and Armbruster, 1987). We also compare the nonlinear analysis to the numerical integration solution using the *ode23* function in *MATLAB*.

3.1. Nondimensionalized equation of motion

The equation of motion given in Eq. (1) can be nondimensionalized by dividing through by kh (cantilever stiffness \times blunt body diameter). Factoring out $A\alpha$ from the expression for C_{FY} in Eq. (2) illustrates how the coefficient A affects the oscillator's linear critical wind speed and how B , C , and D affect its nonlinear behavior such as hysteresis. The resulting nondimensionalized equation of motion and angle of attack are given below:

$$Y'' + 2\zeta Y' + Y = U^2 n A \alpha [1 - \hat{B}\alpha^2 + \hat{C}\alpha^4 - \hat{D}\alpha^6], \quad (6a)$$

$$\alpha = \frac{Y'}{U} - \beta \frac{Yh}{L}, \quad (6b)$$

where Y , Y' , and Y'' are the nondimensional displacement, velocity and acceleration respectively, ζ is the damping ratio, U is the nondimensional wind speed, n is the nondimensional mass, and h is the blunt body characteristic diameter. $\hat{B} = B/A$, $\hat{C} = C/A$, and $\hat{D} = D/A$ are coefficients of the polynomial approximation to C_{FY} normalized for A . Definitions of these parameters in terms of physical parameters are listed in Nomenclature.

3.2. Solution of the equation of motion

With the nondimensionalized equation of motion, Eq. (6), we use the method of harmonic balance in the computer algebra system *WxMaxima* to determine the nondimensionalized oscillator amplitude for a given wind speed. The first step of this calculation is to assume a solution of the form $Y = \bar{Y} \cos(\omega t)$, and substitute that solution into Eq. (6). Here \bar{Y} is the nondimensionalized oscillator amplitude and ω is its frequency. Next we use trigonometric identities to reduce the powers of the sinusoidal terms. By neglecting higher-order harmonics, the coefficients of $\cos(\omega t)$ and $\sin(\omega t)$ can be set equal to zero. This gives two simultaneous algebraic equations on \bar{Y} and ω . We eliminate ω and obtain the following equation on \bar{Y} (Rand and Armbruster, 1987):

$$\begin{aligned} & 35nD\bar{Y}^6 U^6 \gamma^6 + 210\zeta D\bar{Y}^6 U^5 \gamma^5 + 40nC\bar{Y}^4 U^6 \gamma^4 + (105 + 420\zeta^2)nD\bar{Y}^6 U^4 \gamma^4 \\ & + \{160\zeta nC\bar{Y}^4 U^5 + (280\zeta^3 + 420\zeta)nD\bar{Y}^6 U^3\} \gamma^3 + 48nB\bar{Y}^2 U^6 \gamma^2 \\ & + (80 + 160\zeta^2)nC\bar{Y}^4 U^4 \gamma^2 + (105 + 420\zeta^2)nD\bar{Y}^6 U^2 \gamma^2 \\ & + \{96\zeta nB\bar{Y}^2 U^5 + 160\zeta nC\bar{Y}^4 U^3 + 210\zeta nD\bar{Y}^6 U\} \gamma + 64nAU^6 - 128\zeta U^5 \\ & + 48nB\bar{Y}^2 U^4 + 40nC\bar{Y}^4 U^2 + 35nD\bar{Y}^6 = 0, \end{aligned} \quad (7)$$

where $\gamma = \beta h/L$. The comparable expression for the Parkinson and Smith oscillator undergoing pure translation can be found by using the method described above with the nondimensionalized equivalent of Eq. (5) to define the of angle of attack, or equivalently, by substituting the value $\beta=0$ directly into Eq. (7). The result is

$$64nAU^6 - 128\zeta U^5 + 48nB\bar{Y}^2 U^4 + 40nC\bar{Y}^4 U^2 + 35nD\bar{Y}^6 = 0. \quad (8)$$

3.3. Plot the resulting equations

The analytical solutions for steady state amplitude versus wind velocity are plotted and compared to numerical solutions from *MATLAB* in Fig. 2.

3.4. Model comparison

There are two significant observations about the plot in Fig. 2. The first is that both models give the same critical wind speed. The mathematical reason for this can be seen by substituting $\bar{Y} = 0$ into Eqs. (7) and (8). Solving these equations for U gives the same nondimensionalized critical wind speed for both models, namely:

$$U_0 = \frac{2\zeta}{nA}. \tag{9}$$

The other significant observation about these models is that they exhibit different behaviors for large wind speeds. The large wind speed behaviors for both models are independent of the nondimensional parameters n and ζ . They are complicated expressions of $A, \hat{B}, \hat{C}, \hat{D}$. For the oscillator parameters given in the caption of Fig. 2, the Parkinson and Smith purely translational model curve asymptotically approaches a straight line with the equation:

$$\bar{Y} = 0.293U - 0.034. \tag{10}$$

where \bar{Y} is the oscillator's nondimensionalized amplitude and U is the nondimensionalized wind speed. On the other hand, the Cornell–Oudheusden curve for translation coupled with rotation approaches a constant amplitude that is independent of wind speed. This constant amplitude value for an oscillator with a uniform cantilever and parameters given in Fig. 2 caption is shown in Eq. (11a). Eq. (11b) shows the constant amplitude expression for structural designs other than a uniform cantilever, where β is the coefficient relating the structural angle, θ , to displacement, Y ; h is the blunt body diameter; and L is the beam length

$$\bar{Y} = 0.652, \tag{11a}$$

$$\bar{Y} = \frac{0.293}{\beta h/L}. \tag{11b}$$

4. Experimental verification of model

The three purposes of this experiment were to qualitatively verify the Oudheusden–Cornell model, to roughly estimate the coefficients in the the lateral aerodynamic force approximation (Eq. (2)) for a Vibro-wind system, and to determine if trends in these coefficients for different shapes agree with the results of experiments conducted at higher Reynolds numbers. The aerodynamic force approximation for oscillators in the Reynolds number regime $10^3 < Re < 10^4$ is not well established. However, this regime is the range applicable to Vibro-wind oscillator arrays. We adopted a phenomenological model for this experimental investigation and hope future researchers will more rigorously verify these findings.

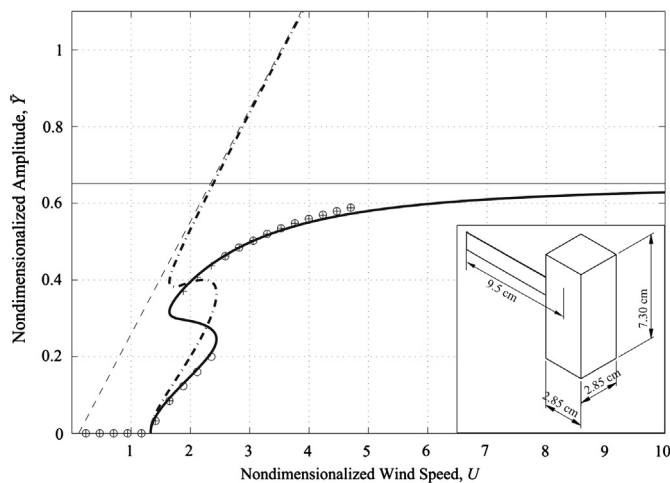


Fig. 2. Bifurcation diagram comparing the Oudheusden–Cornell model to the Parkinson and Smith model for a theoretical oscillator. This simulation used the lateral aerodynamic force approximation coefficients for a square cylinder given by Parkinson and Smith (1964) as $A = 2.69, \hat{B} = 62.5, \hat{C} = 2330,$ and $\hat{D} = 22\,300$. Other parameters used were a natural frequency, ω , of 37 rad/s; damping coefficient, ζ , of 0.022; mass parameter, n , of 0.012; and structural angle coefficient, β , of 1.5. These parameter values are typical for an oscillator with the dimensions shown in the figure. —, Oudheusden–Cornell cantilever model (Eq. (7)); —, Asymptote of the Oudheusden–Cornell cantilever model. \circ , ode23 increasing wind speed; $+$, ode23 decreasing wind speed. — \bullet —, Parkinson and Smith purely translational model (Eq. (8)). — — —, Asymptote of the Parkinson and Smith purely translational model.

4.1. Set-up and procedure

These experiments were performed in a laminar, low-speed, low-turbulence wind tunnel at Cornell University. The test section had a cross section that was 25 cm wide and 25 cm high. The square prism had cross sectional sides of 1.3 cm and a length of 2.0 cm. It was made out of styrafoam that had a density of 27.9 Kg/m^3 . A composite cantilever with a total length of 11.5 cm was inserted about 0.6 cm deep into the rear face of the blunt body, as shown in Fig. 3. The cantilever segment closest to the blunt body was made out of a 0.006 in. thick feeler gage, a steel beam that is commonly used to measure small distances. The feeler gage had a width of 1.3 cm and was cut to 6.4 cm in length. The last 1.3 cm segment length of the feeler gage was glued to the plastic mount of a 303YB Piezo System Standard Double Quick-Mount Piezoelectric Bending actuator. The PZT element was 1.3 cm wide, 0.55 mm thick, and 3.5 cm long. 4.6 mm segments at each end of the PZT element were adhered to plastic mounts. The plastic mount that was not glued to the feeler gage was bolted to an aluminum truss. The truss was weighted down with brass bars to minimize vibrations which otherwise could have affected the experimental results.

A Speedtech WindMate 200 Hand-Held Wind Meter was placed about 25 cm behind the blunt body. The WindMate recorded air flow speeds with an accuracy of one-tenth meter per second. After the oscillator test, a second WindMate was used to verify the accuracy of the first WindMate.

A Polytec ofv-2500 Vibrometer was used to measure blunt body amplitude. The vibrometer was placed about 1.3 m outside of the test section, and its laser was focused on the center of the blunt body side facing the vibrometer. The vibrometer measured amplitude with an accuracy of one-tenth of a millimeter.

The experimental procedure consisted of starting the wind tunnel air flow at a velocity of 1 m/s, which was below the oscillator's critical wind speed. The air flow was increased in increments of 0.1 m/s until the maximum wind speed of 2.8 m/s was reached. Then, the air flow was decreased in increments of 0.1 m/s until the air flow was less than the critical speed and the oscillator stopped vibrating.

4.2. Equation of motion parameters measurement

Oscillator parameters for the nonlinear equation of motion (see Eqs. 1 and 2) such as mass, viscous damping, cantilever stiffness, structural angle for a given displacement, and aerodynamic force coefficients were determined in the following ways.

4.2.1. Measurement of mass

The effective oscillating end mass can be found using two different methods. The first method integrates the kinetic energy of differential mass elements along the length of a beam when mass displacement is based on Euler–Bernoulli beam theory. For a blunt body on a uniform cantilever, this method gives the effective mass as

$$m = m_{\text{BB}} + 0.236m_{\text{cant}} \quad (12)$$

where m_{BB} is the blunt body mass and m_{cant} is the cantilever mass. The coefficient in front of m_{cant} agrees within 3% of the value 0.243 given by the Euler–Bernoulli beam equation for a cantilever undergoing first modal transverse vibration (Inman, 2008). This integrating method could be extended to structural designs other than the uniform cantilever.

A second method was actually used in this experiment because the mass and stiffness of the two plastic mounts on the PZT component were not readily available, and these parameters affect the cantilever's kinetic energy. This method measured the oscillator's natural frequency and cantilever stiffness, and then used those values to calculate the oscillator's

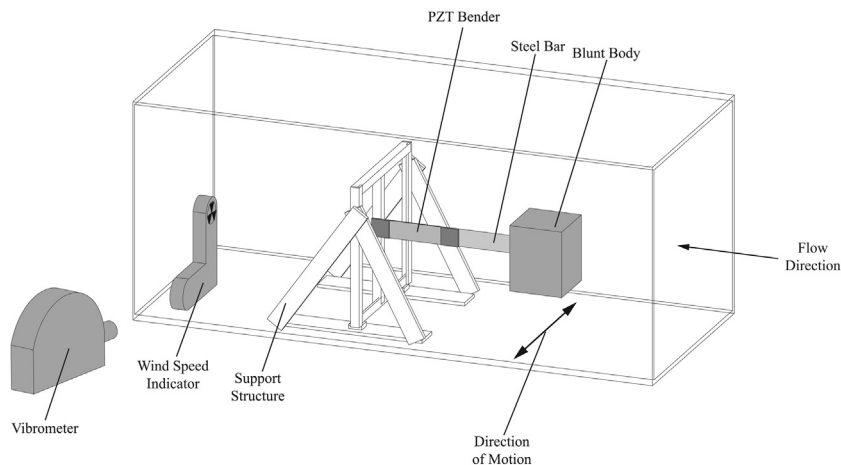


Fig. 3. Experimental set-up.

effective mass. The natural frequency was measured using an oscilloscope in a wind speed of about 2.2 m/s. The cantilever stiffness was measured using the procedure described in Section 4.2.3. Based on the measured natural frequency and cantilever stiffness, the experimental oscillator had an effective mass of 0.21 g. Cantilever and blunt body masses were also measured separately. The square cylinder had a mass of 0.091 g, and the cantilever had a mass of 3.8 g. Based on the experimental effective mass, the square cylinder accounted for 43% of the oscillator's effective mass while the cantilever accounted for 57% of it.

4.2.2. Measurement of viscous damping

The coefficient of viscous damping, r , was measured by recording blunt body displacement versus time after disturbing the blunt body from equilibrium in the absence of any air flow. This was done using the vibrometer described in Section 4.1. The damping was calculated from the envelope function for the decaying oscillations.

4.2.3. Measurement of cantilever stiffness

As mentioned above, the cantilever was a compound structure of a PZT bender and thin elastic steel strip. Cantilever stiffness, k , was determined by hanging known masses from the cantilever when it was clamped to a horizontal beam on a truss. Using this method, it was determined that the cantilever was slightly nonlinear and obeyed the equation $k=2.4(1+11.3y)$, where cantilever stiffness, k , is given in units of N/m, and displacement, y , is given in units of m. For these experiments, the maximum displacement, y , was on the order of 3 mm, so the value of the cantilever stiffness changed by about 3% due to displacement.

4.2.4. Analysis of theoretical structural angle

As described in Section 2, the Oudheusden–Cornell model uses the beam theory of a uniform cantilever to relate blunt body angle to displacement. The resulting equation, Eq. (3), is repeated below:

$$\theta = \frac{3y}{2L} = \beta \frac{y}{L}. \quad (13)$$

For the Vibro-wind oscillator, however, the cantilever consists of two beams in series that have different second moments of inertia, I , and Young's Modulus, E . This dual composition complicates the relationship between structural angle and displacement at the end of the cantilever. Using the boundary conditions of equal displacement, slope, moment, and shear force at the interface between the two beam components, the following equation relating cantilever tip angle to displacement is derived:

$$\theta = \frac{3}{2} \frac{(EI)_g L_p^2 + 2(EI)_g L_g L_p + (EI)_p L_g^2}{(EI)_g L_p^3 + 3(EI)_g [L_g L_p^2 + L_g^2 L_p] + (EI)_p L_g^3} y, \quad (14)$$

where y is blunt body displacement, θ is blunt body structural angle, (EI) is the product of Young's Modulus and the second Moment of Inertia, and L is the length of the beam. The subscripts g and p indicate whether the term refers to the feeler gage steel strip or PZT beam respectively. This analysis neglects effects of the two plastic mounts on the PZT component. Based on typical steel properties and data published by Piezo-Systems, the oscillator described in this experimental section has values of $(EI)_g = 7.754e-4 \text{ N m}^2$, $(EI)_p = 1.933e-3 \text{ N m}^2$, $L_g = 6.35e-2 \text{ m}$, $L_p = 3.18e-2 \text{ m}$, and $L = L_p + L_g = 9.53e-2 \text{ m}$. These values result in a structural angle-displacement relationship of $\theta = 1.74 y/L$. The proportionality constant in this equation differs by about 16% from the value of 1.5 for a uniform cantilever (see Eq. (13)).

4.2.5. Analysis of the aerodynamic force coefficients

The oscillator parameters of mass, viscous damping, and cantilever stiffness were directly measured, but the lateral aerodynamic force versus angle of attack was not. Although both this experiment and Parkinson and Smith's (1964) experiment were for a square cylinder, it is suspected that Parkinson and Smith's coefficients in the polynomial approximating lateral force (see Eq. (2)) do not accurately describe the force for this experiment's Reynolds number. The Parkinson and Smith data was collected at a Reynolds number of 22 300 whereas this experiment's data was collected at Reynolds numbers ranging from 1500 to 2500.

Our wind tunnel lab did not readily have the equipment necessary to measure lateral aerodynamic force directly for varied angles of attack. Therefore, a semi-empirical method was used to determine the coefficients in the lateral aerodynamic force approximation polynomial, $C_{FY} = A\alpha[1 - B\alpha^2 + C\alpha^4 - D\alpha^6]$. As shown in Eq. (9), A could be determined by the oscillator's critical wind speed. Eq. (9) is repeated below with nondimensional critical wind speed replaced by its dimensional equivalent:

$$V_0 = \frac{2\zeta}{nA} \omega h. \quad (15)$$

Having measured critical wind speed, V_0 , viscous damping, ζ , mass parameter, n , frequency, ω , and blunt body diameter, h , Eq. (15) could be solved for A .

The other force coefficients were determined by iterative curve-fits to the experimental data. The effects of different \hat{B} , \hat{C} , and \hat{D} values on a theoretical bifurcation plot's amplitude values and hysteresis region are described in Sections 5.2 and 5.3.

The coefficients found using this analysis are given in the *Cornell* row of Table 1. They are compared to the coefficients found by Parkinson and Smith (1964) and the coefficients derived from data collected by Luo et al. (1993).

4.3. Experimental results

4.3.1. Experimental data for a square cylinder

The three data sets suggest several trends for different flow conditions. One trend is that significantly lower Reynolds numbers and lower aspect ratios l/h cause the force polynomial to have a higher value for A . Comparing the Cornell data to the Parkinson and Smith data, for which both the Reynolds number and the aspect ratio l/h decrease by a factor of 14, A increases by a factor of 3.7. Comparing the Parkinson and Smith data to the Luo data, however, for which the Reynolds number decreases by the smaller factor of 1.5 and the aspect ratio l/h increases by a factor of 2.5, A decreases by a factor of 2.0 instead of increasing. Smaller aspect ratios may affect the flow by making it more three-dimensional. In Table 1, the coefficients \hat{B} , \hat{C} , and \hat{D} are divided by A in order to compare the shape of the C_{FY} versus α curve independently of A , which affects the oscillator's critical wind speed. \hat{B} does not show any trend for decreasing Reynolds number or increasing aspect ratio, l/h . \hat{C} and \hat{D} increase for lower Re .

In addition to changes in the experiment's Reynolds number or aspect ratio, l/h , the dynamic test may have introduced effects that did not occur in the static tests.

4.3.2. Experimental data for a trapezoidal cylinder

Shapes with low critical wind speeds, high amplitude sensitivity, and minimal hysteresis are optimal for a Vibro-wind energy harvester system. These properties depend on the lateral aerodynamic force coefficients, A , \hat{B} , \hat{C} , and \hat{D} . For this reason, it is desirable to identify any trends in A , \hat{B} , \hat{C} , and \hat{D} for different oscillator shapes. Such data has been collected by Luo et al. (1993) for Reynolds numbers exceeding the range applicable to Vibro-wind. Here, we collect data on a trapezoidal cylinder so that we can compare its performance to that of the square in the Vibro-wind Reynolds number regime.

Table 2 shows the force coefficients derived from an experiment similar to the one described in Sections 4.1 and 4.2 for a trapezoidal cylinder. The table compares this experiment's force coefficients to those derived from Luo et al. (1993). The two data sets differ by the Reynolds number in which the data was collected and the aspect ratio, l/h , of the blunt bodies. Both blunt bodies have a rear:front diameter ratio, η , of 0.75, and the streamwise:cross-stream ratios, $depth/h$, differ by only 15%. The two data sets seem to show that as Reynolds number and aspect ratio l/h increase, \hat{B} and \hat{C} increase, while A and \hat{D} remain relatively constant. Reasons for these differences may be the change in flow behavior for different Reynolds numbers, and aspect ratios.

4.3.3. Conclusions from experiment

The data for the square cylinder in Fig. 4 and trapezoidal cylinder in Fig. 5 weakly verify the Oudheusden–Cornell model. The experimental data for the square has a qualitative shape that agrees with the curves made by simulating the Parkinson and Smith and Oudheusden–Cornell models (Eqs. (7) and (8) respectively). The experimental data for the trapezoid has a qualitative shape that agrees well with the model curves for wind speeds less than 5 m/s. Furthermore, the square oscillator exhibited hysteresis for wind speeds greater than the critical wind speed for oscillation, and the trapezoidal oscillator exhibited hysteresis for wind speeds starting at the critical wind speed. The phenomenon of hysteresis is predicted by both the Parkinson and Smith and Oudheusden–Cornell models. The general wind speed ranges in which the hysteresis occurred relative to the critical wind speed agrees with the relative ranges predicted by previous researchers' lateral force coefficients

Table 1

Comparison of coefficients in the lateral aerodynamic force coefficient approximation $C_{FY} = A\alpha[1 - \hat{B}\alpha^2 + \hat{C}\alpha^4 - \hat{D}\alpha^6]$ for a square cylinder found by Parkinson and Smith in a static test, fitted to Luo data from a static test, and by the present authors in a semi-empirical curve-fit to dynamic test data.

	A	$\hat{B} = B/A$	$\hat{C} = C/A$	$\hat{D} = D/A$	Re	Aspect ratio l/h
Based on Luo et al. (1993)	5.50	38.0	1260	12 400	34 000	9.2
Parkinson and Smith (1964)	2.69	62.5	2330	22 300	22 300	23
Cornell	10.0	55.0	3900	70 000	1000–2300	1.6

Table 2

Comparison of coefficients in the lateral aerodynamic force coefficient approximation $C_{FY} = A\alpha[1 - \hat{B}\alpha^2 + \hat{C}\alpha^4 - \hat{D}\alpha^6]$ based on data from a static test by Luo et al. (1993) and a semi-empirical curve-fit to dynamic data collected by the present authors for a trapezoidal cross section.

	A	$\hat{B} = B/A$	$\hat{C} = C/A$	$\hat{D} = D/A$	Re	Aspect ratio l/h	Streamwise: Cross-Stream ratio $depth/h$
Trapezoid 1 (Luo et al., 1993)	2.79	30.3	444	1790	34 000	9.2	1
Cornell	2.70	1.85	167	1850	6000–8000	1.5	0.85

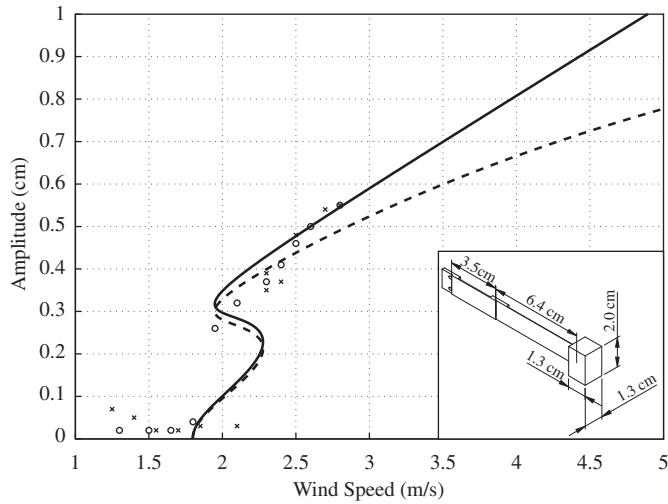


Fig. 4. Comparison of theory and experimental data for a square cylinder. Both models use the aerodynamic force coefficients given in the *Cornell* row of Table 1. This oscillator had a natural frequency, ω , of 108 rad/s; damping coefficient, ζ , of 0.0095; and mass parameter, n , of $1.4e-3$. — — Oudheusden–Cornell cantilever model (Eq. (7)). —, Parkinson and Smith purely translational model (Eq. (8)); +, experimental data – increasing wind speed. o, experimental data – decreasing wind speed.

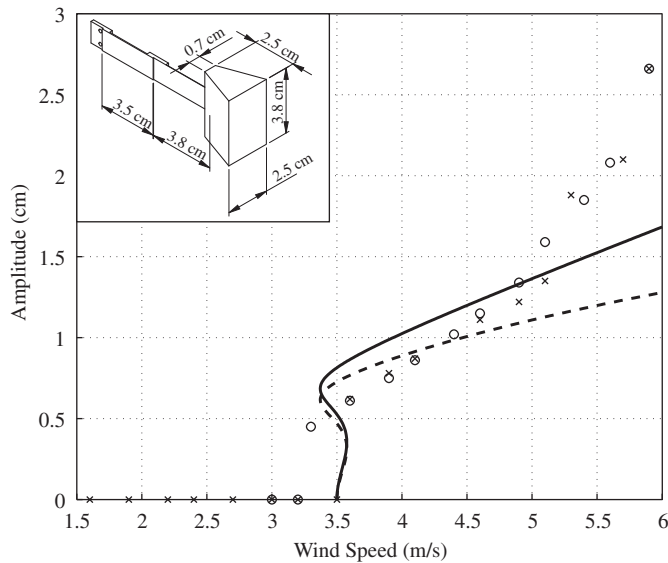


Fig. 5. Experimental data for a trapezoidal section. These coefficients are comparable to the Luo coefficients for a trapezoid with $\eta = 0.75$. This oscillator had a natural frequency, ω , of 130 rad/s; damping coefficient, ζ , of 0.0123; and mass parameter, n , of 0.0085. — —, Oudheusden–Cornell cantilever model (Eq. (7)); —, Parkinson and Smith purely translational model (Eq. (8)); +, experimental data – increasing wind speed; o, experimental data – decreasing wind speed.

for similar shapes (Luo et al., 1993; Parkinson and Smith, 1964). In the high wind speed regime, however, the square cylinder experimental data does not seem to confirm either model over the other, and the trapezoid experimental data does not agree with either model.

As mentioned in Section 4.2.5, this data can be used to roughly estimate the aerodynamic force coefficients of cylinders with lower aspect ratios and in lower Reynolds number flows. Low Re and small aspect ratios are characteristics of the low wind speeds and small blunt bodies used by Vibro-wind. These factors may make the lateral aerodynamic force coefficient A and coefficient ratios \hat{B} , \hat{C} , and \hat{D} have different values than those derived from previous experiments, which were conducted for larger Reynolds numbers and aspect ratios. Parkinson and Smith noted that lower Reynolds numbers shift the peak of the C_{FY} versus α curve to the left (Parkinson and Smith, 1964). Luo et al. (2003) have also used a 2-D hybrid vortex computation scheme to numerically investigate why lowering the Reynolds number shifts the inflection point in the C_{FY} versus α curve to a lower value of α . The peak of the C_{FY} versus α curve for both the Cornell square and Cornell trapezoid shifts to the left when compared to the Parkinson and Smith (1964) and Luo et al. (1993) data for the same shape in a higher

Re. The Cornell square data was collected at Reynolds numbers 21 and 14 times respectively smaller than that of the Luo or Parkinson and Smith data. The Cornell trapezoid was collected at a Reynolds number 5 times smaller than the Luo trapezoid data. The trend of a left-shifting peak C_{FY} for decreasing Re, however, is not observed for the decrease in Re of only 1.5 between the Luo and Parkinson and Smith square data.

Several observations can be made when comparing the aerodynamic coefficients of the square and trapezoidal blunt bodies tested in this experiment. First, the square cylinder has a larger A value than the trapezoid. As shown in Eq. (9), shapes with larger A values have lower critical wind speeds. Second, using each shape's force coefficients to plot its corresponding C_{FY} versus α curve, we see that the square cylinder's curve has a higher peak value, which corresponds to higher amplitude sensitivity than the trapezoid. This means that if the square and trapezoid cylinders were the same size and had the same viscous damping and mass, the square would oscillate with larger amplitudes than the trapezoid. Third, when nondimensionalized and normalized for the damping coefficient and mass parameter, the square cylinder also has a smaller range of wind speeds with hysteresis than the trapezoidal cylinder. These trends in critical wind speed, amplitude sensitivity, and hysteresis agree with the trends based on (Luo et al., 1993) for higher Reynolds numbers and aspect ratios.

In the next section, we will explore the possibility of optimizing aerodynamic force constants to decrease critical wind speed, increase amplitude sensitivity, and diminish amplitude hysteresis in the flow behavior.

5. Blunt body shape optimization

Blunt body size and cross section shape affect its performance in a Vibro-wind energy harvesting system. Here, good performance is defined as a blunt body with a low critical wind speed, high amplitude sensitivity to wind speed, and minimal hysteresis during galloping. This section discusses how blunt body shape and size play a role in these three components of performance. The characteristics of a theoretical optimal oscillator are described. The discussion uses the performance of a square cylinder with the lateral aerodynamic force coefficients found by Parkinson and Smith (1964).

5.1. Critical wind speed for oscillation

As described in Section 3.4, the solution to the nonlinear differential equation modeling the oscillator can be solved to determine the oscillator's critical wind speed, V_0 , required for galloping to begin. Eq. (9) is dimensionalized and repeated below:

$$V_0 = \frac{2r}{hl\rho A}. \quad (16)$$

Eq. (16) shows that critical wind speed can be minimized by decreasing viscous damping, r ; increasing the blunt body frontal area to wind direction, hl ; and increasing the aerodynamic force approximation coefficient, A . Viscous damping depends on blunt body shape and increases with blunt body size. Since both the frontal area, hl , and viscous damping, r , increase with blunt body size, one would need to determine which variable is more sensitive to changes in blunt body size. If for a given increase in blunt body size, hl increases more than r , then the critical wind speed will be reduced. The aerodynamic force coefficient, A , in Eq. (2) depends on the shape of the blunt body. The value of A for different shapes has been extensively studied (e.g. Alonso and Meseguer, 2006; Luo et al., 1998). As can be seen by differentiating Eq. (2), A is the slope of the lateral aerodynamic force coefficient when angle of attack α equals 0:

$$A = \left. \frac{dC_{FY}}{d\alpha} \right|_{\alpha=0}. \quad (17)$$

The blunt body is unstable if A is positive (Blevins, 1990).

5.2. Amplitude sensitivity to wind speed

Another constraint on the lateral force polynomial approximation coefficients is that the oscillator have a high amplitude sensitivity to wind speed. One way to implement this constraint is to require that the lateral aerodynamic force coefficients meet an arbitrary peak value on the C_{FY} versus α curve because larger peak C_{FY} values correspond to larger amplitudes (see Fig. 7). As can be seen in the equation for the lateral aerodynamic force versus angle of attack, Eq. (2), $C_{FY} = A\alpha[1 - \hat{B}\alpha^2 + \hat{C}\alpha^4 - \hat{D}\alpha^6]$, the values of the C_{FY} curve increase as the magnitudes of A and \hat{C} increase. They decrease as the magnitudes of \hat{B} and \hat{D} increase. The order of decreasing sensitivity of the peak value to changes in these coefficients is \hat{C} , \hat{D} , A , and \hat{B} . The computer algebra program *WxMaxima* was used to symbolically solve for the peak C_{FY} value in Eq. (2) and set the peak to a value between 0 and 1. Fig. 6 depicts the relationship between coefficients \hat{B} , \hat{C} , and \hat{D} , such that the peak C_{FY} value equals 0.6. This peak value was selected because it represents a slightly higher amplitude sensitivity to wind speed than that of a square cylinder, which has a peak C_{FY} value of 0.57 based on the coefficients found by Parkinson and Smith (1964).

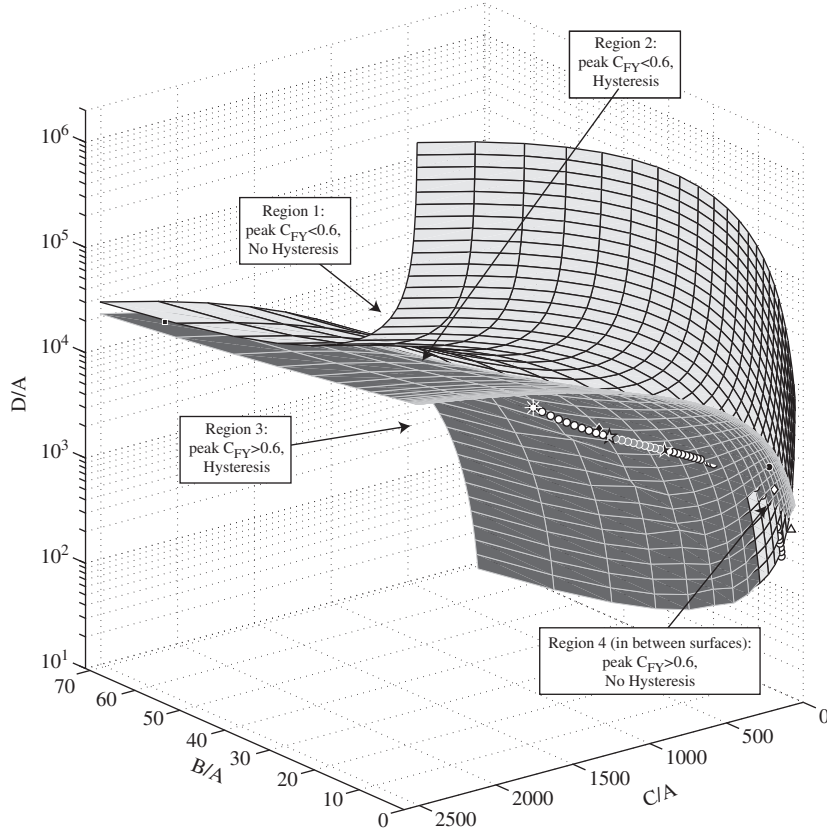


Fig. 6. Three-dimensional plot of surfaces with no hysteresis and a desired maximum C_{FY} value. Increasing the assumed A value of the *peak* C_{FY} surface shifts it upwards along the D/A axis. , *peak* C_{FY} surface: Surface for which the peak value of the C_{FY} curve is 0.6 and A is 2.69. , *no hysteresis surface*: Surface for which hysteresis has been eliminated. ■, square (Parkinson and Smith, 1964); •, Cornell Trapezoid (see Table 2); △, coefficients based directly on Luo et al.'s (1993) data for a triangle ($\eta = 0$): Overrepresented *peak* C_{FY} value ($A = 2.0$), ○, Luo trend, $0.1 \leq \eta \leq 0.7$, and $0.8 \leq \eta \leq 0.9$: Skewed depiction relative to *peak* C_{FY} surface. ◇, Coefficients directly based on Luo et al.'s (1993) data for a trapezoid: $\eta = 0.5$: Overrepresented *peak* C_{FY} value ($A = 1.6$), ★, Luo trend: $\eta = 0.7$, ●, Luo trend: $0.7 < \eta < 0.8$, ☆, Luo et al.'s (1993) trend: $\eta = 0.8$, ♦, Coefficients directly based on Luo et al.'s (1993) data: $\eta = 0.75$, ■, Luo trend: $\eta = 0.9$: Underrepresented *peak* C_{FY} value ($A = 4.2$).

5.3. Hysteresis minimization

The final constraint on the lateral aerodynamic force approximation coefficients is that the oscillator exhibit minimal hysteresis. This requirement is imposed because practical wind energy harvesting will occur in a variable wind environment, and with hysteresis, one would not know which bifurcation branch the oscillator would end up on. It is better to minimize hysteresis and eliminate it if possible.

For this purpose, we solved Eq. (7) for the starting and ending wind speeds of the hysteresis region as a function of the oscillator parameters. We did this using the computer algebra program *WxMaxima*. First, we set the derivative of Eq. (7) with respect to \bar{Y} equal to 0. This equation was then combined with Eq. (7) in order to eliminate \bar{Y} . The final equation is a quadratic on U , and its two roots are the nondimensionalized wind speeds for which hysteresis begins and ends (i.e. the local extrema in Fig. 2 for $U(\bar{Y})$). Using the quadratic formula on the final equation, the nondimensionalized wind speeds when hysteresis starts and ends obey the following equation:

$$U_{Hysteresis} = \frac{(13230\hat{D}^2 - 3780\hat{B}\hat{C}\hat{D} + 800\hat{C}^3)\zeta \pm \zeta\sqrt{80(20\hat{C}^2 - 63\hat{B}\hat{D})^3}}{nA(6615\hat{D}^2 - 3780\hat{B}\hat{C}\hat{D} + 800\hat{C}^3 + 756\hat{B}^3\hat{D} - 180\hat{B}^2\hat{C}^2)}, \quad (18)$$

where ζ is the reduced damping coefficient, n is the mass parameter, and A , \hat{B} , \hat{C} , and \hat{D} , are the lateral force coefficients.

The hysteresis region is eliminated when the discriminant of Eq. (18) is equal to or less than 0. When the discriminant equals 0, the starting and ending wind speeds equal each other, and the local maximum and minimum in the curve of U versus \bar{Y} (as shown in Fig. 8) become a single inflection point. The discriminant equals 0 and hysteresis vanishes when

$$\frac{\hat{B}\hat{D}}{\hat{C}^2} \geq 0.318. \quad (19)$$

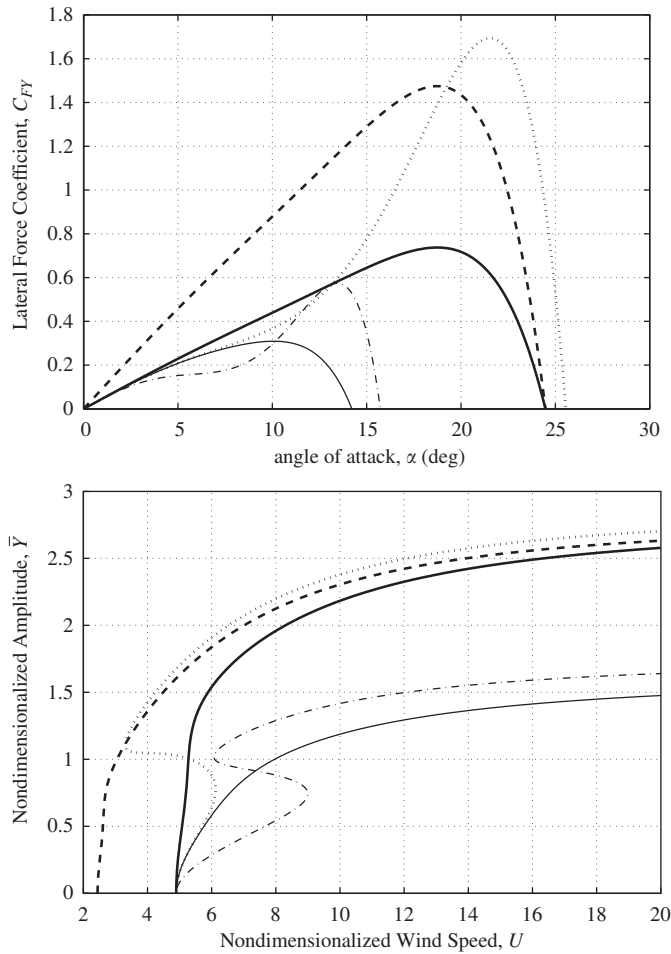


Fig. 7. (Top) C_{FY} versus α for blunt bodies with force coefficients in different regions of Fig. 6. (Bottom) The corresponding nondimensionalized amplitude versus wind speed diagrams for parameter values of natural frequency, $\omega = 108$ rad/s, damping coefficient, $\zeta = 0.0095$, and mass parameter, $n = 1.4e-3$. — Region 1: $A = 2.69, \hat{B} = 17.6, \hat{C} = 391, \hat{D} = 6.00e3$. - • - Region 2: square cylinder (Parkinson & Smith, 1964): $A = 2.69, \hat{B} = 62.5, \hat{C} = 2330, \hat{D} = 2.3e4$. •••• Region 3: $A = 2.69, \hat{B} = 17.6, \hat{C} = 391, \hat{D} = 1.65e3$. — — — — Region 4: $A = 2.69, \hat{B} = 3.65, \hat{C} = 62.5, \hat{D} = 397$. — — — — Region 4 when larger A value: $A = 5.38, \hat{B} = 3.65, \hat{C} = 62.5, \hat{D} = 397$.

The findings from this analysis are that the existence of hysteresis depends only on the parameters \hat{B} , \hat{C} , and \hat{D} , for any oscillator.

When the hysteresis region does exist, values of parameters in Eq. (18) affect its size and location. For typical force coefficient values, increasing the magnitude of \hat{B} or \hat{D} shifts the hysteresis region to higher wind speeds and decreases the range of wind speeds with hysteresis. Increasing the magnitude of \hat{C} shifts the hysteresis region to lower wind speeds and increases the range of wind speeds with hysteresis. \hat{B} , \hat{C} , and \hat{D} values can be changed by altering a blunt body's shape.

According to Eq. (18), the midpoint and range of nondimensional wind speeds in the hysteresis region are both proportional to the nondimensional group ζ/nA , or (reduced damping coefficient)/(mass parameter $\times A$). When this expression is dimensionalized, the midpoint and range of wind speeds in the hysteresis region are proportional to r/hl , where r is the viscous damping, and hl is the blunt body's frontal area to the wind direction. Thus, the location and size of the hysteresis region can be adjusted by changing the blunt body shape (which changes A and viscous damping) or its size (which changes frontal area and viscous damping). Additional significance to the hysteresis midpoint and range both being proportional to ζ/nA is that changing a parameter in this group can reduce hysteresis and shift it to lower wind speeds, or increase hysteresis and shift it to higher wind speeds. However, such a change cannot both decrease the size of the region and shift it to higher wind speeds. Also, since the expression ζ/nA is the same nondimensional group that appears in the expression for critical wind speed (see Eq. (9)), adjusting these parameters to shift the hysteresis region also shifts the critical wind speed by a proportional amount. Furthermore, the expression ζ/nA is independent of oscillator natural frequency, or, its mass and cantilever stiffness, which signifies that changing the oscillator natural frequency does not affect the hysteresis region or critical wind speed.

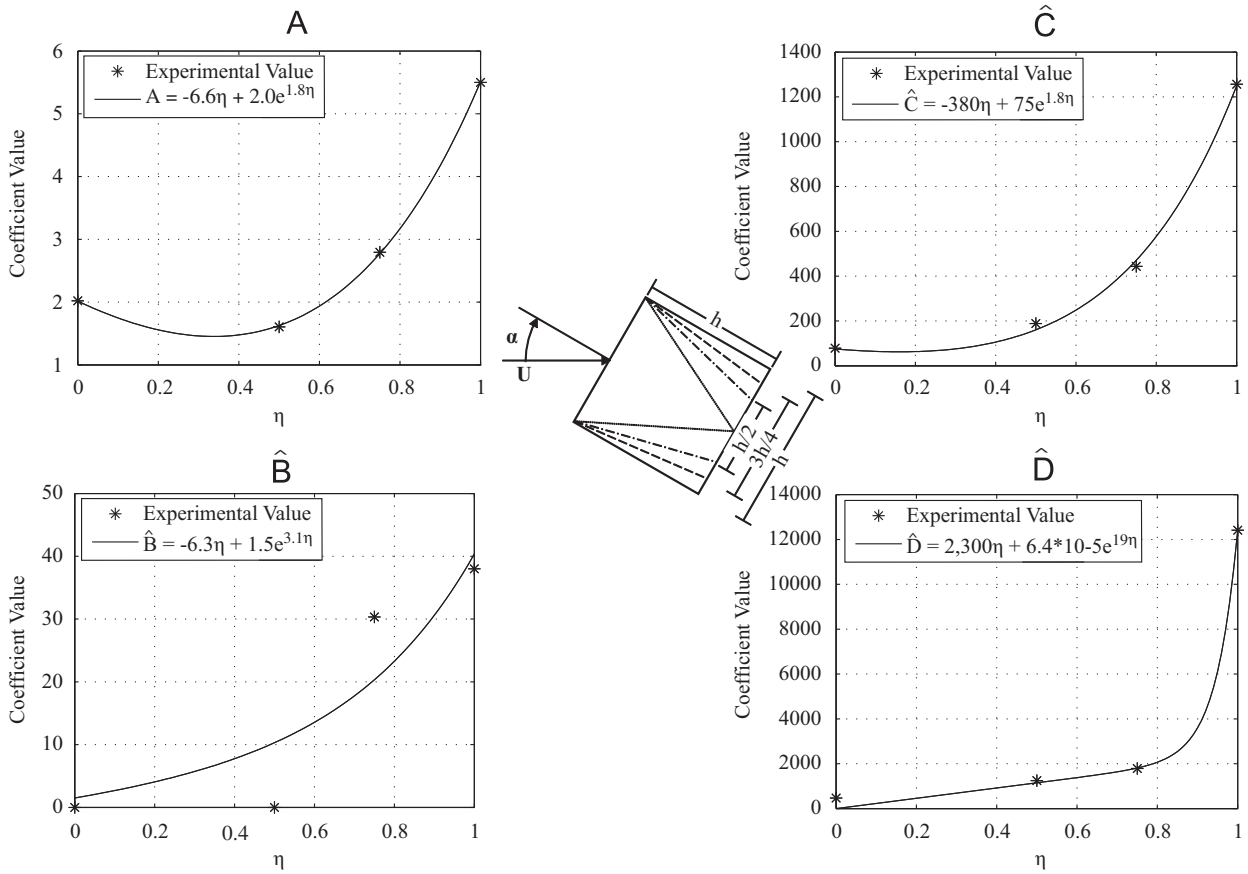


Fig. 8. Trends in lateral force coefficients as η , the ratio of rear diameter:front diameter, changes from 0 to 1, where $\eta=0$ represents a triangle and $\eta=1$ represents a square. Fractional η 's represent trapezoids. The data shown here supports the concept of a continuum of aerodynamic force coefficients corresponding to varying shape dimensions. These force coefficients are based on data collected by Luo et al. (1993) for blunt bodies with cross section dimensions shown in the center image. These shapes include —, square; - - - -, trapezoid 1; - • -, trapezoid 2; ••••, triangle, for which $d=50$ mm.

5.4. Findings relating geometry to performance

The three subsections above describe how blunt body cross sectional shape affects the oscillator's critical wind speed, amplitude sensitivity to wind speed, and hysteresis region. If one assumes a continuum of shapes corresponding to a continuous variation of constants A , \hat{B} , \hat{C} , and \hat{D} , then one can search in this design space for shapes that satisfy the three design criteria. Evidence of a such a continuum is discussed in Section 5.4.1. Fig. 6 shows values of \hat{B} , \hat{C} , and \hat{D} in \hat{B} - \hat{C} - \hat{D} - space that eliminate hysteresis or satisfy the peak C_{FY} requirement.

As shown in Fig. 6, the lateral force coefficients of a blunt body can fall into one of four regions. Regions above the *peak* C_{FY} surface have lower amplitude sensitivity while regions below the surface have higher amplitude sensitivity. Regions above the *No Hysteresis* surface do not have a hysteresis region while regions below the surface do have a hysteresis region. Therefore, the optimal blunt body lies in the region above the *No Hysteresis* surface and below the *peak* C_{FY} surface. Although not clearly visible in the figure, a small optimal region occurs after the surfaces cross for small \hat{B} , \hat{C} , and \hat{D} values. This region is labeled as Region 4. Fig. 7 plots the C_{FY} versus α curves and \dot{Y} versus U curves for blunt bodies in each region.

The spatial relationship of these two surfaces depicts a general trade-off between large amplitude sensitivity and minimal hysteresis. This trade-off is supported mathematically. As discussed in Section 5.2 and shown in Eq. (2), $C_{FY} = A\alpha[1 - \hat{B}\alpha^2 + \hat{C}\alpha^4 - \hat{D}\alpha^6]$; the peak C_{FY} value of a blunt body increases if the magnitudes of A and \hat{C} increase and decreases if the magnitudes of \hat{B} and \hat{D} increase. This means that for a blunt body with a given A value, larger peak C_{FY} values occur for smaller ratios of $\hat{B}\hat{D}:\hat{C}^2$. On the other hand, Eq. (19) shows that hysteresis is eliminated for $\hat{B}\hat{D}:\hat{C}^2 \geq 0.318$. That is, hysteresis is minimized for larger ratios of $\hat{B}\hat{D}:\hat{C}^2$. As shown in Eqs. (2) and (18), larger A values both increase the peak C_{FY} value and minimize the size of the hysteresis region. For an A value of 2.69, relatively small \hat{B} , \hat{C} , and \hat{D} values satisfy the requirements for large amplitude sensitivity and minimal hysteresis, as indicated by Region 4 in Fig. 6. In this optimal region, $\hat{B}\hat{D}:\hat{C}^2$ is only slightly larger than 0.318 so that hysteresis is just eliminated and the peak C_{FY} value is just above 0.6.

The location of the *peak* C_{FY} surface in this figure depends on both the arbitrary peak value desired for the C_{FY} versus α curve and the assumed value of A (Fig. 6 assumes a value of A because there are four force coefficients, but only three axes

may be drawn.). As shown in Eq. (2), $C_{FY} = A\alpha[1 - \hat{B}\alpha^2 + \hat{C}\alpha^4 - \hat{D}\alpha^6]$, the peak value of the C_{FY} versus α curve is directly proportional to A when all other coefficients stay constant. Increasing the assumed value of A while keeping the desired peak C_{FY} value constant would make the peak C_{FY} surface appear to shift upwards along the \hat{D} axis, increasing the size of the optimal Region 4. Effectively, if A increases, then \hat{B} must increase, \hat{C} must decrease, or \hat{D} must increase to satisfy the peak value. Conversely, the effect of increasing the desired peak C_{FY} value while keeping the assumed value of A constant is to shift the peak C_{FY} surface downwards.

Fig. 6 shows the peak C_{FY} surface for a peak C_{FY} value of 0.6 and an A value of 2.69. For the reasons described in the previous paragraph, the peak C_{FY} surface is inaccurately plotted relative to the experimental \hat{B} , \hat{C} , and \hat{D} values if the experimental A values greatly differ from the assumed A value of the peak C_{FY} surface. $A = 2.69$ was chosen for the peak C_{FY} surface in Fig. 6 because that is the approximate A value for the Parkinson and Smith square blunt body, Cornell trapezoid, and Luo trapezoid 1 (see Tables 1 and 2).

The coefficients for the square cylinder found by Parkinson and Smith (1964) lie below the *No Hysteresis* and above the peak C_{FY} surface, in Region 2. That is, the square cylinder has a low amplitude sensitivity and a hysteresis region. Coefficients for all other shapes and experimental conditions described in this paper fall in Region 3, which has a higher amplitude sensitivity than Region 2 but also exhibits hysteresis. These shapes include two trapezoidal cylinders with rear:front diameter ratios, η , of 0.75 as listed in Table 2. They also include a trapezoidal cylinder with $\eta = 0.5$ and a triangle ($\eta = 0$) based on data collected by Luo et al. (1993) that is discussed in Section 5.4.1. Fig. 6 slightly overrepresents the distances of these two shapes from the peak C_{FY} surface, meaning that Fig. 6 implies larger peak C_{FY} values, because the shapes' actual A values are less than the assumed A value of the peak C_{FY} surface. Although all in Region 3, some of these shapes, such as the Cornell trapezoid, are closer to the optimal Region 4 than others.

Fig. 6 also plots the trend in \hat{B} , \hat{C} , and \hat{D} values suggested by Luo et al.'s (1993) data as a blunt body cross section transitions from a triangle to a square. This trend is discussed in detail in Section 5.4.1. The A values of this trend are within 10% of 2.69 for $0.7 \leq \eta \leq 0.8$, where η is the ratio of the cross sectional rear:front diameter as shown in Fig. 8. Therefore, the depiction of this trend with respect to the peak C_{FY} surface in Fig. 8 is fairly accurate for these values of η . For plotted segments of the trend corresponding to $0.1 \leq \eta \leq 0.7$ and $0.8 \leq \eta \leq 0.9$, $A(\eta)$ differs by more than 10% from 2.69, and Fig. 6 skews the quantitative relationship of the trend's coefficients with respect to the peak C_{FY} surface. For $\eta = 0.1$, Fig. 6 overrepresents the peak C_{FY} value by 55%. For $\eta = 0.9$, Fig. 6 underrepresents the peak C_{FY} value by 35%. However, these data points are included because they accurately depict the suggested qualitative performance of the trend.

In addition to suggesting the blunt body geometry for improved energy harvester performance, the trends in lateral aerodynamic force coefficients fitted to Luo's data support the idea that there is a continuum of shapes corresponding to gradual variations in constants A , \hat{B} , \hat{C} , and \hat{D} and that one can search in this design space for shapes that satisfy the three design criteria (Luo et al., 1993). Experimental studies supporting the shape continuum concept are described in the next section.

5.4.1. Data supporting a continuum of lateral force coefficients

The previous section describes aerodynamic force approximation coefficients that minimize hysteresis and satisfy amplitude sensitivity to wind speed. That discussion assumes that continuously changing a blunt body shape continuously changes its aerodynamic force coefficients. Here, previous experimental studies that describe the coefficients of gradually adjusted blunt body shapes are shown to support this continuum concept. These studies also suggest which shapes in the continuum have optimal coefficient values.

Luo et al. (1993) measured the lateral aerodynamic force coefficient, C_{FY} , versus angle of attack, α , for blunt bodies with incrementally decreased rear diameters (see Fig. 8). The four shapes tested by Luo occupy a parameter space in which a square is at one extreme, a triangle is at the other extreme, and two trapezoids are intermediate shapes. The data collected by Luo can be fitted to the polynomial, $C_{FY} = A\alpha[1 - \hat{B}\alpha^2 + \hat{C}\alpha^4 - \hat{D}\alpha^6]$. Fig. 8 shows how the coefficients in this equation varied for each shape. The force coefficients for increasing rear diameter:front diameter ratio, η , in Fig. 8 can be fitted to functions that sum one linear and one exponential term. The way in which these experimental coefficients seem to follow a pattern suggests that a coefficient-shape continuum does exist and can be exploited to optimize blunt body performance.

Luo's studies have shown that different blunt body shapes are unstable for different ranges of α , have different peak C_{FY} values, and show varying amounts of hysteresis (Luo et al., 1993, 1998). His data shows that the range of α for which the blunt body is unstable (that is, $dC_{FY}/d\alpha > 0$) increases as the cylinder becomes less square (that is, η decreases). It also shows that hysteresis tends to decrease and the peak C_{FY} value tends to increase as η decreases. As discussed in Section 5.2, larger peak C_{FY} values correlate to larger blunt body amplitudes for a given wind speed.

The trends fitted to Luo's data in Fig. 8 suggest that for $0 < \eta < 0.15$ and $0.6 < \eta < 1$, cylinders have high amplitude sensitivity and exhibit hysteresis. Since A is larger for $\eta > 0.6$, these cylinders also have lower critical wind speeds. Additionally, although cylinders for $\eta > 0.85$ have hysteresis, the amount of hysteresis decreases as η increases. For, $0.15 \leq \eta \leq 0.6$, cylinders have lower amplitude sensitivity and no hysteresis. The trade-off between higher amplitude sensitivity or less hysteresis, as discussed in Section 5.4, makes the optimal cylinders occur for the η values in which hysteresis has just disappeared (that is, $\hat{B}\hat{D}/\hat{C}^2 = 0.318$). Such η values include $\eta = 0.15$, $\eta = 0.6$, and $\eta = 1$. Since the value of A is larger for $\eta \geq 0.6$, the optimal rear:front diameter values may be $\eta = 0.6$ or $\eta \approx 1$, which represent square-like trapezoids.

Further evidence supporting a continuum of shape coefficients is provided by Alonso and Meseguer (2006). Alonso has experimentally determined trends in the instability of isosceles triangle blunt bodies for varied main vertex angle, δ , angle of

attack, α , and radius of curvature for rounded corners. He recorded aerodynamic lift and drag for nine triangular cross sections with main vertex angle, δ ranging from 10° to 90° and for three triangular cross sections with varied radii of curvature. The aerodynamic lift and drag coefficients are related to the lateral force coefficient discussed in this paper by $dC_{FY}/d\alpha = dC_L/d\alpha + C_D$ (Den Hartog, 1956). When the blunt body initial angle of attack, α_0 , is set equal to 0, then A in the approximation of C_{FY} (see Eq. (2)) satisfies the equation $A = (dC_L/d\alpha + C_D)|_{\alpha=0}$.

Alonso determined that there is a range of initial angle of attacks, α_0 , for which a triangular blunt body is unstable, and that this range can be approximated as $\alpha_0 = \pm(\delta/2 + 5^\circ)$. The magnitude of A varies within this range of α_0 . Alonso explains that A decreases as the main vertex angle, δ , increases, and A approaches 0 for $\delta = 70^\circ$. Furthermore, as the blunt body corners become more rounded, the range of range of α_0 for which the blunt body is unstable decreases, but the magnitude of A increases.

Trends in Alonso's experimental data not only support the concept of a shape-force coefficient continuum, but they suggest that triangular blunt bodies with main vertex angle values between $30^\circ \leq \delta \leq 50^\circ$, rounded corners, and possibly a nonzero initial angle of attack will have the largest A values out of the shapes he considered. Angles of $30^\circ \leq \delta \leq 50^\circ$ correspond to the same angles between front and side cross sectional edges as trapezoids with rear:front diameter ratios of $0.46 \geq \eta \geq 0.07$.

6. Summary and conclusion

This paper analyzed the nonlinear dynamics of a transverse galloping blunt body oscillator with respect to its geometric shape and size for the purpose of scavenging energy from the wind. The Oudheusden model for galloping, which applies to a blunt body oscillating on a hinged bar, was extended to a blunt body oscillating on a cantilevered beam, the current mechanism used by the Cornell Vibro-wind energy harvesting system. The amplitude of a galloping oscillator that couples rotation with translation is always less than the amplitude of an oscillator that moves in pure translation. For a blunt body with coupled translation and rotation, the vibration amplitude reaches a horizontal asymptote with increasing wind speed. For a purely translational blunt body model, however, the amplitude continues to increase linearly with increasing wind speed. The degree to which the rotation is coupled with the translation affects the oscillator's maximum attainable amplitude. Therefore, the ideal connecting mechanism would minimize the blunt body's rotation as it oscillates.

Experimentally, this paper investigated the effects of a lower Reynolds number on the oscillator's lateral aerodynamic force coefficients. This was done by using nonlinear dynamics analysis to fit the data to the aerodynamic force model. Few experiments have been conducted at the Reynolds numbers in which Vibro-wind operates, $10^3 < Re < 10^4$. The coefficient values based on data from Alonso and Meseguer (2006), Luo et al. (1993), and Parkinson and Smith (1964) were from experiments conducted at $Re > 10^4$. In their paper, Parkinson and Smith noted that lower Reynolds numbers shift the peak of the C_{FY} versus α curve to the left (Parkinson and Smith, 1964). Making use of the data available, this paper assumed that the performance trends among different blunt body shapes remains the same for different Reynolds numbers. Experiments conducted by these authors supported this assumption. Future tests of lateral aerodynamic force versus angle of attack could be used to further verify it.

The main purpose of this paper was to theoretically determine the blunt body shape that optimizes a galloping oscillator's performance. This paper showed that optimal combinations of lateral aerodynamic force coefficients A , \hat{B} , \hat{C} , and \hat{D} minimize the critical wind speed for instability, increase the sensitivity of amplitude to wind velocities beyond the critical speed, and minimize or eliminate amplitude hysteresis for increasing and decreasing wind speeds. Analysis of the coefficients showed that the hysteresis region is shifted to higher wind speeds and its wind speed range is minimized and even eliminated for large ratios of $\hat{B}\hat{D} : \hat{C}^2$. Amplitude sensitivity to wind speed, quantified by the peak C_{FY} value, increases with \hat{C} and decreases with \hat{B} and \hat{D} . This suggests a general trade-off between minimizing hysteresis and increasing amplitude sensitivity. Additionally, the midpoint and length of the hysteresis region and the critical wind speed for oscillation to begin are all proportional to the nondimensional group, ζ/nA (proportional to *viscous damping/frontal area*). Amplitude sensitivity is inversely proportional to ζ/nA . While amplitude sensitivity increases for smaller oscillator natural frequencies, hysteresis and critical wind speed are independent of natural frequency.

This analysis assumed that there is a continuum of force coefficients for continuously adjusted shapes. Previous experimental evidence supports the continuum concept and existence of a shape that satisfies the lateral aerodynamic force performance requirements. Experimental data from Luo et al. (1993) suggests that the coefficients A , \hat{B} , \hat{C} , and \hat{D} adjust on a continuum as blunt body cross sectional shape changes from a square to a triangle. Experimental data from Alonso and Meseguer (2006) suggests that A adjusts on a continuum as the main vertex of an equilateral triangular cylinder changes from a small angle to a large angle. Based on these data sets, the blunt body that would perform best for a Vibro-wind energy harvester would be a trapezoidal prism with a rear:front diameter ratio of $\eta \approx 0.15$, $\eta \approx 0.55$, or $\eta \approx 1$, have rounded corners, and possibly have a nonzero initial angle of attack. Previous Vibro-wind studies have found that blunt bodies that are generally trapezoidal like but have truncated corners at the frontal edge (i.e. they are actually irregular hexagons with right angles between front and side cross sectional edges) oscillate at lower critical wind speeds and show less hysteresis than square blunt bodies (Moon, 2010a).

References

- Alonso, G., Meseguer, J., 2006. A parametric study of the galloping stability of two-dimensional triangular cross section bodies. *Journal of Wind Engineering and Industrial Aerodynamics* 94, 241–253.
- Barrero-Gil, A., 2010. Energy harvesting from transverse galloping. *Journal of Sound and Vibration* 329, 2873–2883.
- Barrero-Gil, A., Sanz-Andrés, A., Alonso, G., 2009. Hysteresis in transverse galloping: the role of the inflection points. *Journal of Fluids and Structures* 25, 1007–1020.
- Blevins, R.D., 1990. In: *Flow-Induced Vibration*, second ed. Van Nostrand Reinhold, New York.
- Bryant, M., Garcia, E., 2011. Modeling and testing of a novel aeroelastic flutter energy harvester. *Journal of Vibration and Acoustics* 133, 011010.
- Den Hartog, J.P., 1956. In: *Mechanical Vibrations*, fourth ed. McGraw-Hill, New York.
- Erturk, A., Vieira, W.G.R., De Marqui Jr., C., Inman, D.J., 2010. On the energy harvesting potential of piezoaeroelastic systems. *Applied Physics Letters* 96, 184103.
- Frayne, S.M., 2008. Generator Utilizing Fluid-Induced Oscillations. United States of America, Patent No. US2008129254.
- Inman, D.J., 2008. In: *Engineering Vibration*, third ed. Pearson Prentice Hall, Upper Saddle River, NJ.
- Kuroda, M., Moon, F.C., 2007. Experimental reconsideration of spatio-temporal dynamics observed in fluid-elastic oscillator arrays from a complex system point of view. *Journal of Complexity* 12, 36–47.
- Li, S., Lipson, H., 2009. Vertical-stalk flapping-leaf generator for parallel wind energy harvesting. In: *Proceedings of AMSE/AIAA Conference on Smart Materials and Adaptive Structures*. Oxnard, California, pp. 1276.
- Luo, S.C., Chew, Y.T., Ng, Y.T., 2003. Hysteresis phenomenon in the galloping oscillation of a square cylinder. *Journal of Fluids and Structures* 18, 103–118.
- Luo, S.C., Chew, Y.T., Yazdani, M.G., 1998. Stability to translational galloping vibration of cylinders at different mean angles of attack. *Journal of Sound and Vibration* 215, 1183–1194.
- Luo, S.C., Yazdani, M.G., Chew, Y.T., Lee, T.S., 1993. Effects of incidence and afterbody shape on flow past bluff cylinders. *Journal of Wind Engineering and Industrial Aerodynamics* 53, 375–399.
- McKinney, W., DeLaurier, J.D., 1981. Wingmill—an oscillating-wing windmill. *Energy* 5, 109–115.
- Moon, F., 1992. *Chaotic and Fractal Dynamics: an Introduction for Applied Scientists and Engineers*. Wiley, New York.
- Moon, F.C., 2010a. Principles of Nonlinear Vibro-Wind Energy Conversion. In: Hutter, K., Wu, T., Shu, Y. (Eds.), *From Waves in Complex Systems to Dynamics of Generalized Continua*, World Scientific, Hackensack, New Jersey, pp. 385–401.
- Moon, F.C., 2010b. Vibro-wind energy technology for architectural applications. Accessed 4/28/2013 (<http://www.windtech-international.com/articles/vibro-wind-energy-technology-for-architectural-applications>).
- Novak, M., ASCE, M., Tanaka, H., 1974. Effect of turbulence on galloping instability. *ASCE Journal of the Engineering Mechanics Division* 100, 27–47.
- Parkinson, G.V., Smith, J.D., 1964. The square prism as an aeroelastic non-linear oscillator. *The Quarterly Journal of Mechanics and Applied Mathematics* 17, 225–239.
- Rand, R.H., 2012. Lecture Notes on Nonlinear Vibrations. Accessed 8/15/2012 (<http://ecommons.library.cornell.edu/handle/1813/28989>).
- Rand, R.H., Armbruster, D., 1987. *Perturbation Methods, Bifurcation Theory, and Computer Algebra*. Springer-Verlag, New York.
- Tang, L., Paidoussis, M.P., DeLaurier, J.D., 2008. Flutter-Mill: A New Energy-Harvesting Device. Accessed 8/15/2012 (http://64.34.71.154/Storage/26/1817_Flutter-Mill-_a_New_Energy-Harvesting_Device.pdf).
- Van Oudheusden, B.W., 1995. On the quasi-steady analysis of one-degree-of-freedom galloping with combined translational and rotational effects. *Nonlinear Dynamics* 8, 435–451.